

Electronic structure study of the intermetallic compound $GdRhIn_5$

Yulu He(贺宇璐), Bo Wang(王博), Xiangfei Yang(杨向飞), Dengpeng Yuan(袁登鹏), Wei Feng(冯卫), Yaobo Huang(黄耀波), and Qiuyun Chen(陈秋云)

Citation: Chin. Phys. B, 2026, 35 (**3**): 037101. DOI: 10.1088/1674-1056/ae3123
http://cpb.iphy.ac.cn; http://iopscience.iop.org/cpb

What follows is a list of articles you may be interested in

Unconventional superconductivity in Cr-based nitride $La_3Cr_{10-x}N_{11}$

M Y Zou(邹牧远), J C Jiao(焦嘉琛), K W Chen(陈锴文), C Y Jiang(姜程予), C S Chen(陈长胜), X Li(李鑫), Q Wu(吴琼), N Y Zhang(张宁远), O O Bernal, P C Ho, A Koda, D E MacLaughlin, and L Shu(殳蕾)

Chin. Phys. B, 2025, 34 (**11**): 117104. DOI: 10.1088/1674-1056/ae001a

Magnetism, heat capacity, magnetocaloric effect, and magneto-transport properties of heavy fermion antiferromagnet CeGaSi

Li-Bo Zhang(张黎博), Qing-Xin Dong(董庆新), Jian-Li Bai(白建利), Qiao-Yu Liu(刘乔宇), Jing-Wen Cheng(程靖雯), Cun-Dong Li(李存东), Pin-Yu Liu(刘品宇), Ying-Rui Sun(孙英睿), Yu Huang(黄宇), Zhi-An Ren(任治安), and Gen-Fu Chen(陈根富)

Chin. Phys. B, 2024, 33 (**6**): 067101. DOI: 10.1088/1674-1056/ad3060

Electronic structure study of the charge-density-wave Kondo lattice $CeTe_3$

Bo Wang(王博), Rui Zhou(周锐), Xuebing Luo(罗学兵), Yun Zhang(张云), and Qiuyun Chen(陈秋云)

Chin. Phys. B, 2023, 32 (**9**): 097103. DOI: 10.1088/1674-1056/acb41e

$CeAu_2In_4$: A candidate of quasi-one-dimensional antiferromagnetic Kondo lattice

Meng Lyu(吕孟), Hengcan Zhao(赵恒灿), Jiahao Zhang(张佳浩), Zhen Wang(王振), Shuai Zhang(张帅), and Peijie Sun(孙培杰)

Chin. Phys. B, 2021, 30 (**8**): 087101. DOI: 10.1088/1674-1056/ac0a60

Possible nodeless $s^{\pm}$-wave superconductivity in twisted bilayer graphene

Zhe Liu(刘哲), Yu Li(李宇), Yi-Feng Yang(杨义峰)

Chin. Phys. B, 2019, 28 (**7**): 077103. DOI: 10.1088/1674-1056/28/7/077103

RAPID COMMUNICATION

Electronic structure study of the intermetallic compound $GdRhIn_5$

Yulu He(贺宇璐)[1,†], Bo Wang(王博)[1,†], Xiangfei Yang(杨向飞)[1,†], Dengpeng Yuan(袁登鹏)[1], Wei Feng(冯卫)[1], Yaobo Huang(黄耀波)[2], and Qiuyun Chen(陈秋云)[1,‡]

[1] *Science and Technology on Surface Physics and Chemistry Laboratory, Mianyang* 621907, *China*
[2] *Shanghai Institute of Applied Physics, Chinese Academy of Sciences, Shanghai* 201204, *China*

(Received 21 November 2025; revised manuscript received 22 December 2025; accepted manuscript online 25 December 2025)

Heavy-fermion compounds frequently host emergent phases — most notably non-BCS superconductivity and unconventional quantum criticality — whose microscopic origins can invariably be traced to the entanglement of itinerant and nearly localized electronic degrees of freedom. In this work, we carry out a systematic study on the electronic structure and quasiparticle features of the antiferromagnetic intermetallic compound $GdRhIn_5$, utilizing high-resolution angle-resolved photoemission spectroscopy (ARPES) measurements. Energy-dependent measurements reveal the coexistence of Fermi surface topologies with both quasi-two-dimensional and three-dimensional characteristics. Notably, the quasiparticle bands commonly observed in conventional cerium-based compounds are absent from the resonance data, likely due to the strong localization nature of the Gd 4f states within the compound. Temperature-dependent studies, combined with density functional theory (DFT) calculations, demonstrate that as temperature decreases, the electronic density of states (EDC) near the Fermi level increases, while the peak position of the MDC associated with the β energy band shows a shrinking trend. This systematic exploration of $GdRhIn_5$'s electronic structure enhances our comprehension of the microscopic physical properties not only of $GdRhIn_5$ but also of the broader family of rare-earth-based 115 systems.

Keywords: heavy fermion, 4f-electron, electronic structure, localized-itinerant

PACS: 71.27.+a, 72.15.Rn, 79.60.–i, 71.20.Eh

DOI: 10.1088/1674-1056/ae3123 **CSTR:** 32038.14.CPB.ae3123

1. Introduction

Materials featuring f-electron systems have long held the interest of researchers, owing to their intricate many-body phenomena, including heavy fermion states, unconventional superconductivity, and quantum critical transitions.[1–6] The collective hybridization between localized f-electrons and conduction electrons gives rise to composite quasiparticles, characterized by substantially enhanced effective masses and expanded Fermi surface volumes.[7] The ground-state properties of f-electron systems are governed by the competitive interplay between Kondo hybridization and the Ruderman–Kittel–Kasuya–Yosida (RKKY) interaction.[8–10] Notably, the dual localized–itinerant character of f-electrons enables their simultaneous participation in both superconducting pairing and competing ordered states.[11] Thus, a comprehensive understanding of the exotic behaviors in f-electron systems necessitates detailed elucidation of their electronic structures via advanced spectroscopic investigations.

The $RMIn_5$ system constitutes a family of intermetallic compounds, predominantly composed of rare-earth elements (R) with 4f electronic configurations, paired with transition metals (M) from the Co, Rh, and Ir groups. These materials exhibit a broad spectrum of electronic and magnetic phenomena, encompassing heavy fermion behavior, unconventional superconductivity, and complex magnetic states.[12–20] Such properties are closely tied to the strong electronic correlations in R 4f orbitals and the quasi-two-dimensional nature of their Fermi surfaces. Particularly striking manifestations of these phenomena are observed in cerium-based compounds within this system.[21–24]

The compound investigated herein, $GdRhIn_5$, adopts the prototypical $HoCoGa_5$-type tetragonal crystal structure and undergoes antiferromagnetic ordering at a Néel temperature (T_N) of 40.0 K.[25] Consistent with ^{155}Gd Mössbauer spectroscopy data, resonant x-ray diffraction measurements on $GdRhIn_5$ reveal a simple collinear antiferromagnetic structure, where Gd magnetic moments are aligned in or near the basal plane.[26] Temperature-dependent magnetic susceptibility [$\chi(T)$] measurements exhibit a distinct transition at 40 K, indicative of the onset of long-range antiferromagnetic ordering.[27] In the paramagnetic regime, the susceptibility follows Curie–Weiss behavior, with an effective magnetic moment ($\mu_{\rm eff}$) of 8.40 $\mu_{\rm B}$ and a paramagnetic Curie temperature $\theta_{\rm p}$ of -70 K.[28–31] Specific heat measurements disclose a sharp anomaly at the corresponding ordering temperature, which can be successfully modeled using the Heisenberg model — considering only the first-nearest-neighbor

[†]These authors contributed equally to this work.
[‡]Corresponding author. E-mail: sheqiuyun@126.com
© 2026 Chinese Physical Society and IOP Publishing Ltd. All rights, including for text and data mining, AI training, and similar technologies, are reserved.

coupling (J).[32] In contrast to compounds such as $CeRhIn_5$ and $CeCoIn_5$, detailed studies of the electronic structure of $GdRhIn_5$ remain relatively scarce.

Previously, both theoretical and experimental investigations into a series of gadolinium-based intermetallic compounds have consistently demonstrated that the 4f electrons of gadolinium exhibit strong localization characteristics. For instance, in Gd_2Co_2Al,[33] LSDA + U (local spin density approximation with Hubbard U) calculations yield an extremely sharp, localized Gd 4f peak near the Fermi level. In FP-LAPW (full-potential linearized augmented plane wave) studies of Gd$Au$$X$ (where X = Mg, Cd, In),[34] a narrow Gd 4f peak is identified at −4.3 eV, which is explicitly characterized as "localized and non-bonding" — reinforcing the lack of significant hybridization with conduction bands. Even under extreme conditions, such as 100 GPa of hydrostatic pressure, FP-LAPW calculations on elemental gadolinium show that the 4f states remain sharp and localized, with only minimal energy shifts; this confirms the robust localization of Gd 4f electrons even under high compression.[35] In magnetic analyses of Gd_2Co_{17},[36] researchers further assume localized Gd 4f magnetic moments that couple indirectly via conduction electrons — a model that aligns closely with experimental observations, providing additional evidence for 4f localization. For the Gd$M$$In_5$ family (M = Co, Rh, Ir), GGA + U (generalized gradient approximation with Hubbard U) calculations[37] adopt a Hubbard U value of 6 eV for the Gd 4f shell. The authors justify this parameter choice by stating that the strong localization of the 4f electrons makes GGA + U appropriate. Despite the extensive research that has been conducted on the Ce-based 115 systems, investigations into Gd-based 115 systems — particularly studies focusing on their electronic structures — remain unreported.

In the present study, we successfully synthesized the tetragonal compound $GdRhIn_5$ via the flux method and systematically investigated its electronic structure. Utilizing high-resolution ARPES, we acquired well-resolved Fermi surfaces and complete band structures. These experimental results were then compared with DFT calculations that treated Gd 4f electrons as localized — revealing two key findings: the coexistence of quasi-two-dimensional and three-dimensional Fermi surface topologies, and the strong localization of Gd 4f states in $GdRhIn_5$. Temperature-dependent electronic structure measurements demonstrate that: while the spectral weight associated with Gd 5d and In 5p orbitals diminishes with increasing temperature, the localized nature of Gd 4f electrons remains unchanged. Consistent with our measured resonance data, no heavy quasiparticle bands nor significant f–c hybridization behavior were observed near the Fermi level across the entire temperature range investigated. Concurrently, the peak position of the MDC near the β energy band shows an increasing trend. This phenomenon is attributed to enhanced spin fluctuations near T_N, which introduce additional scattering for conduction electrons and drive a redistribution of spectral weight from coherent to incoherent components. This temperature evolution originates from the modulation of scattering by magnetic fluctuations in the context of localized 4f electrons, rather than from heavy-fermion behavior.

2. Experimental details

Single crystals of $GdRhIn_5$ were grown using a self-flux method with high-purity elemental constituents: Gd (99.9%), Rh (99.95%), and In (99.999%). The starting materials were combined in a non-stoichiometric ratio of Gd:Rh:In = 1:1:20 and loaded into an alumina crucible. This crucible assembly was then sealed inside a quartz tube under an argon atmosphere to prevent oxidation during heating. The crystal growth process employed a three-stage thermal program: (1) heating to 1150 °C, followed by a 10-hour isothermal hold to ensure complete melting and homogenization of the precursor mixture; (2) controlled cooling at a rate of 10 °C/h to 750 °C, a step optimized to promote nucleation and oriented crystal growth; (3) gradual temperature reduction at 1 °C/h down to 450 °C, minimizing thermal stress to avoid crystal cracking. After growth, residual flux was removed by centrifuging the quartz tube at the final growth temperature,[38] a standard technique to isolate high-quality single crystals from the molten In flux.

Chemical composition of the as-synthesized $GdRhIn_5$ single crystals was verified using energy-dispersive spectroscopy (EDS). Structural characterization was carried out via x-ray diffraction (XRD) measurements using a PANalytical X'Pert Pro diffractometer with Cu $K\alpha$ radiation, which confirmed the compound's tetragonal $HoCoGa_5$-type structure. Electrical transport properties were investigated over the temperature range of 2–300 K using a physical property measurement system (PPMS). The ARPES data presented in this work were acquired at the BL09U "Dreamline" beamline of the Shanghai Synchrotron Radiation Facility (SSRF), using a Scienta DA30 electron analyzer. The measurements were performed with an energy resolution of 17 meV and an angular resolution of 0.2°. The samples were cleaved along the c-axis at 18 K under ultrahigh vacuum conditions before performing the ARPES measurements. Throughout the measurement process, the base pressure of the system was maintained below 2×10^{-10} mbar.

The electronic band structures and Fermi surfaces of $GdRhIn_5$ were computed using the Vienna *Ab initio* Simulation Package (VASP) in conjunction with the projected augmented-wave potential (PAW) method. The exchange–correlation interactions were treated within the generalized gradient approximation (GGA). The 4f electrons of Gd

were put in the frozen core. Structural relaxations were performed using the conjugate gradient algorithm with a plane-wave cutoff energy of 520 eV. A Gamma-centered k-point grid of $7\times7\times1$ was used for sampling the Brillouin zone. The convergence criterion for ionic steps was set to a maximum force on any atom below 0.01 eV/Å.

3. Results and discussion

The $GdRhIn_5$ crystal exhibits lattice parameters of $a = b = 4.606$ Å and $c = 7.439$ Å.[37] As illustrated in the ball-and-stick model of the crystal structure [Fig. 1(a)], the compound crystallizes in a tetragonal lattice, which can be described as alternating $RhIn_2$ and $GdIn_3$ planes stacked along the c-axis. The transition metal Rh — acting as a linker between adjacent $GdIn_3$ planes — plays a critical role in stabilizing the material's low-temperature phase.[37] Figure 1(b) presents the corresponding Brillouin zone in the reciprocal space, with the center plane (Γ–M–X at $k_z = 0$) and boundary plane (Z–A–R at $k_z = \pi/c$) explicitly labeled. Through periodic fitting of k_z-dependent ARPES data, we determined the characteristic photon energies required to probe these planes: 84 eV for the center plane and 102 eV for the boundary plane. The experimental configuration for our ARPES measurements is schematically depicted in Fig. 1(c). Linear horizontal (LH) polarization is oriented perpendicular to the plane defined by the sample surface normal and the analyzer slit, while the linear vertical (LV) polarization lies parallel to this plane.[39] The XRD patterns in Fig. 1(d) demonstrate that the natural cleavage plane corresponds to the (001) crystallographic orientation. The absence of impurity-related diffraction peaks further verifies the high crystalline quality of the flux-grown $GdRhIn_5$ single crystals. Figure 1(e) shows the core-level spectrum measured at $h\nu = 108$ eV. Within the 0–60 eV binding energy range, dominant peaks are observed, which correspond to the Gd 4f and In 4d core states. These spectral features are

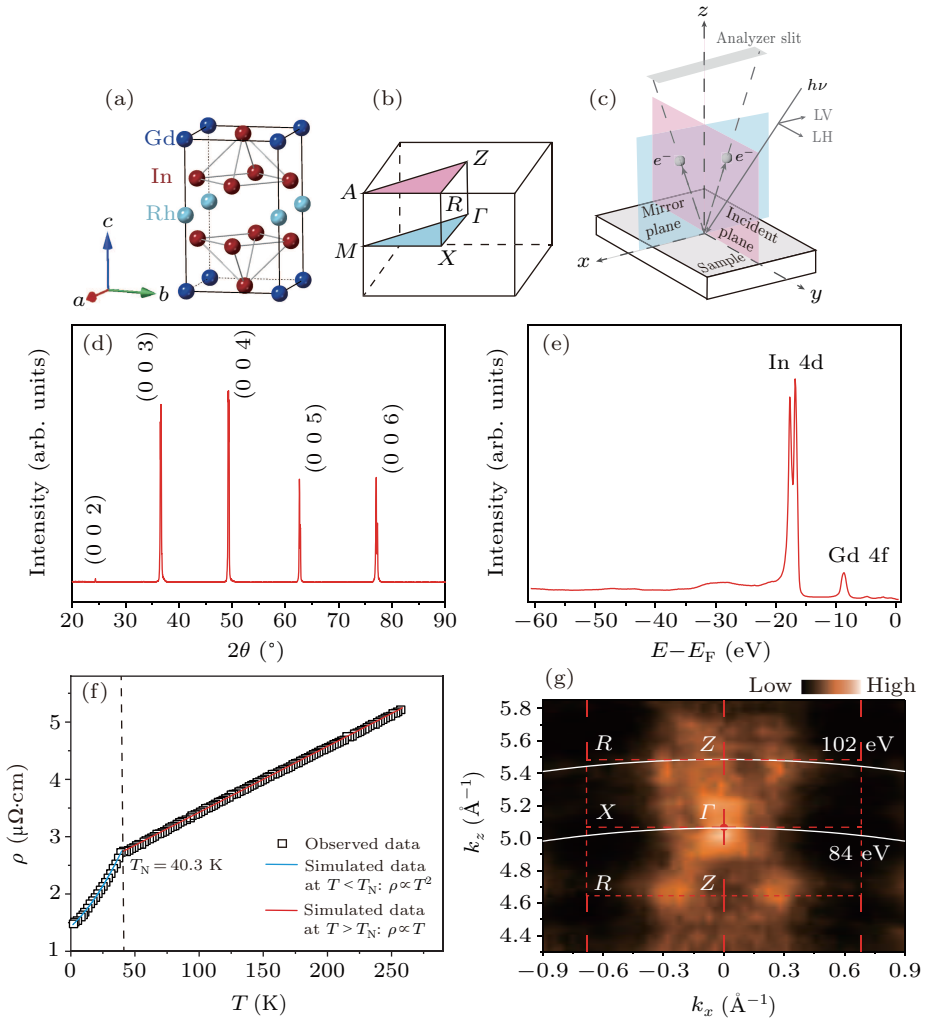


Fig. 1. (a) Crystal structure of $GdRhIn_5$. Gd, In and Rh atoms correspond to blue, red and cyan spheres in the bat model, respectively. (b) The Brillouin zone (BZ) of $GdRhIn_5$. (c) Experimental setup utilized for ARPES measurements. (d) Single-crystal XRD data of $GdRhIn_5$. Only sharp (0 0 1) peaks can be observed. (e) The core energy level of $GdRhIn_5$ measured at $T = 12$ K using photon energy $h\nu = 108$ eV. (f) The temperature dependence of resistivity shows an obvious kink in the curve at $T = 40.3$ K. (g) The photoelectron intensity map in the Γ–X–R–Z plane, photon energy range is 54 eV to 123 eV. In the case of an internal potential $V = 17$ eV, the relative position of the first Brillouin zone is indicated by the red box. The momentum cuts made at 102 eV and 84 eV have been marked with white lines, which pass through the Z and Γ points, respectively.

consistent with prior x-ray photoelectron spectroscopy (XPS) measurements on Gd–In intermetallic compounds,[40,41] confirming the material's chemical identity. Temperature-dependent resistivity measurements [Fig. 1(f)] reveal a distinct kink at the Néel temperature ($T_N = 40.3$ K), which aligns with the resistivity transition temperature reported by Pagliuso *et al.*[25] Below T_N, the resistivity follows a power law behavior ($\rho \propto T^2$), indicative of dominant Fermi liquid-like scattering in the antiferromagnetically ordered metallic state.[42] In the paramagnetic regime, the linear temperature dependence originates primarily from electron–phonon interactions.[26,27] In the ARPES experiments, the in-plane momentum ($k_{\parallel}$) can be determined through the momentum conservation principle in photoemission processes,[43] while the out-of-plane momentum (k_z) is accessible by varying the incident photon energy[44,45] — a standard approach for mapping 3D electronic structures. Figure 1(g) presents the photoelectron intensity map along the Γ–X–R–Z plane acquired at 7 K. Unless explicitly stated otherwise, all ARPES data in this work were collected at this base temperature to minimize thermal broadening of the spectral features. Based on the Brillouin zone geometry and the measured dispersion of bands along the k_z direction, we estimate the inner potential of $GdRhIn_5$ to be 17 eV. However, due to k_z-broadening effects, it was not possible to resolve the precise dispersion relations of some specific bands, such as the α band, along the k_z direction.

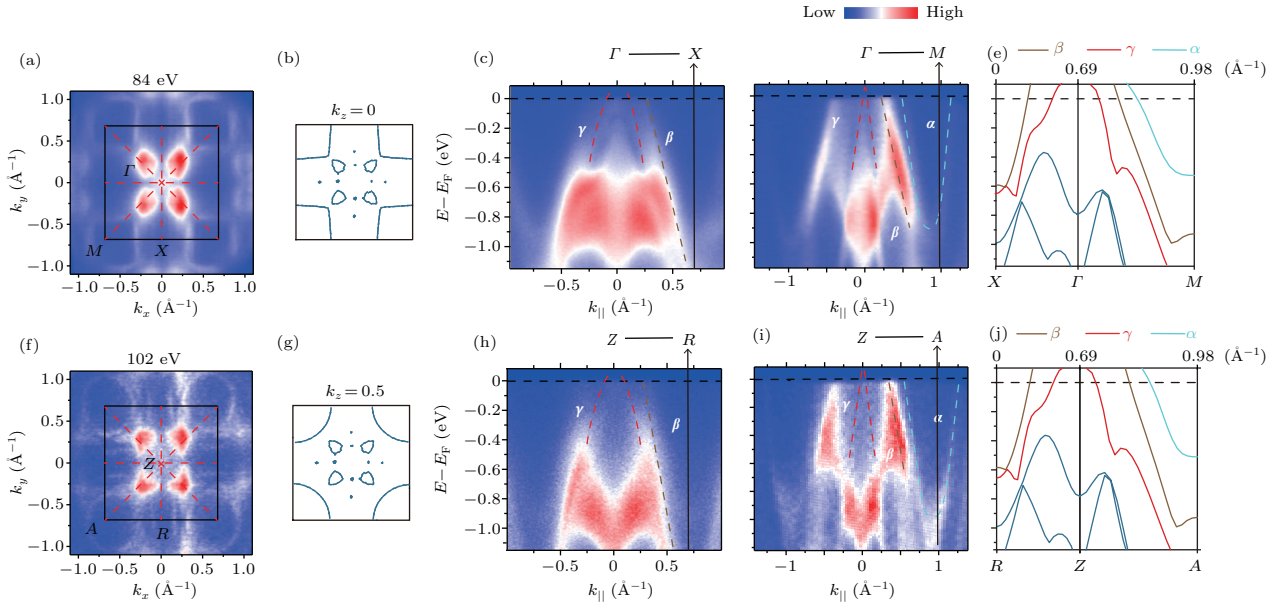


Fig. 2. (a) Experimental Fermi surface (FS) maps in the k_x–k_y plane, acquired using 84 eV photons (corresponding to $k_z \approx 0$, the center plane of the Brillouin zone). The intensity integration window is set to $E_F \pm 50$ meV to isolate states crossing the Fermi level. (b) Calculated Fermi surface of $GdRhIn_5$ at $k_z = 0$, obtained from DFT simulations treating Gd 4f electrons as localized. (c)–(d) Experimental photoemission intensity distributions along the high-symmetry paths (c) Γ–X and (d) Γ–M (both at $k_z \approx 0$). Bright regions correspond to high spectral weight of electronic states, with E_F marked as the reference energy. (e) Calculated valence band structure of $GdRhIn_5$ along Γ–X and Γ–M, overlaid with the same energy scale as the experimental data in panels (c)–(d) for direct comparison. (f) Experimental k_x–k_y Fermi surface maps acquired using 102 eV photons (corresponding to $k_z \approx 0.5$, the boundary plane of the Brillouin zone). The intensity integration window is identical to (a) ($E_F \pm 50$ meV). (g) Calculated Fermi surface of $GdRhIn_5$ at $k_z = 0.5$, matching the k_z condition of the experimental data in panel (f). (h)–(i) Experimental photoemission intensity distributions along the high-symmetry paths (h) Z–R and (i) Z–A, with E_F indicated as the zero-energy reference. (j) Calculated valence band structure of $GdRhIn_5$ along Z–R and Z–A, aligned to the energy scale of panels (h)–(i) to facilitate comparison between calculation and experiment.

The three-dimensional electronic structure of $GdRhIn_5$ was measured by ARPES, with the experimental results compared directly to DFT calculations. Figures 2(a) and 2(f) present the Fermi surfaces of the Γ–M–X plane (center plane, $k_z \approx 0$) and the Z–A–R plane (boundary plane, $k_z \approx 0.5\ \pi/c$), measured at photon energies of 84 eV and 102 eV, respectively. Black squares in these panels denote the projections of the Brillouin zone onto the corresponding planes; this visualization reveals excellent alignment between the FS contours and BZ boundaries in both planes, alongside distinct fourfold rotational symmetry — consistent with the tetragonal crystal structure of $GdRhIn_5$. Experimental band structures along high-symmetry directions (corresponding to the photon energies above) are displayed in Figs. 2(c)–2(d) and 2(h)–2(i). Characteristic electronic bands are explicitly labeled in these panels to clarify the connection between the Γ–M–X and Z–A–R planes, thereby mapping the 3D dispersion of bands along the k_z direction. The FS topology in the Γ–M–X plane [Fig. 2(a)] reveals four primary pockets. A small square-shaped hole pocket centered at the Γ point, formed by the prominent hole-like γ band along the Γ–X path. A larger square hole pocket surrounding the Γ point, arising from the combined contributions of the β bands. A square electron pocket encircling each M point, derived from the electron-

like α band along the Γ–M path. Two symmetric small rectangular electron pockets located outside each X point. The FS of the Z–A–R plane [Fig. 2(f)] is similar, with differences including a circular electron pocket centered at each A point, formed by the α band; additional spindle-shaped electron pockets adjacent to the circular A-centered pockets. Notably, the experimental band structure of the α band [Figs. 2(d) and 2(i)] shows a consistent V-shaped dispersion in both the Γ–M (Γ–M–X plane) and Z–A (Z–A–R plane) directions. However, the shape of the electron pockets formed by this α band differs drastically between the two planes — reflecting the 3D nature of the FS. A key experimental consideration is the influence of k_z-broadening: compared to the DFT-calculated FSs [Figs. 2(b) and 2(g)], the experimental ARPES spectra exhibit additional spectral weight contributions. These extra features originate from electronic states at adjacent k_z positions, which are blurred into the measured plane due to k_z-broadening (a common artifact in ARPES arising from finite photon coherence and surface inhomogeneities).[46] Furthermore, orbital-resolved calculations presented in Fig. S1 of the supplemental material confirm that the quasiparticle bands near the Fermi level are predominantly composed of Gd 5d, Rh 4d, and In 5p orbitals, with negligible contribution from Gd 4f states.

Prior studies have established that Gd 4f electrons in gadolinium-based intermetallic compounds typically exhibit strong localization characteristics[33–37] — and our ARPES measurements of $GdRhIn_5$ further corroborate this finding. The FS and band structure calculations presented in Fig. 2 were obtained via DFT calculations, using a theoretical framework that treats Gd 4f electrons as fully localized. These DFT results show good qualitative agreement with our experimental ARPES data; this consistency directly confirms that the Gd 4f electrons in $GdRhIn_5$ are indeed in a highly localized state. Nevertheless, minor discrepancies between the DFT calculations and our experimental results remain. Most notably, along the Γ–X and Γ–M directions, the shape and momentum position of the γ band near the Γ point (see Fig. 2(e)) do not fully align with the experimental features shown in Figs. 2(c)–2(d). Such deviations are commonly reported in ARPES studies and are likely attributed to a combination of factors not fully captured in the present theoretical framework, including many-body interactions, surface relaxation effects, spinorbit coupling, and the inherent limitations of the adopted exchange-correlation functional.[47]

Figure 3 presents high-resolution ARPES measurements along the Γ–X direction under selected photon energies. A striking feature is the energy-dependent behavior of the γ band: it is clearly resolved at 87 eV but becomes undetectable at other energies (63 eV and 111 eV), a signature of its three-dimensional character. In contrast, the β band persists across the entire photon energy range with a consistent in-plane momentum distribution, indicative of quasi-two-dimensional behavior. Quantitative analysis via momentum distribution curves (MDCs) in Fig. 3(g) confirms this distinction: well-defined Fermi momentum peaks are observed for the β band across all energies (marked by the arrows), whereas the γ band exhibits a distinct peak only at 87 eV. Further evidence for dimensionality comes from comparing Figs. 2(a) and 2(f): the dispersion intensity at the Z point (probed at 102 eV) is substantially weaker than at the Γ point (87 eV), reinforcing the 3D nature of the γ band and the quasi-2D character of the β band along the k_z direction. These band dimensionality characteristics are consistent with those observed in $CeRhIn_5$,[48] highlighting a structural analogy within the 115 family.

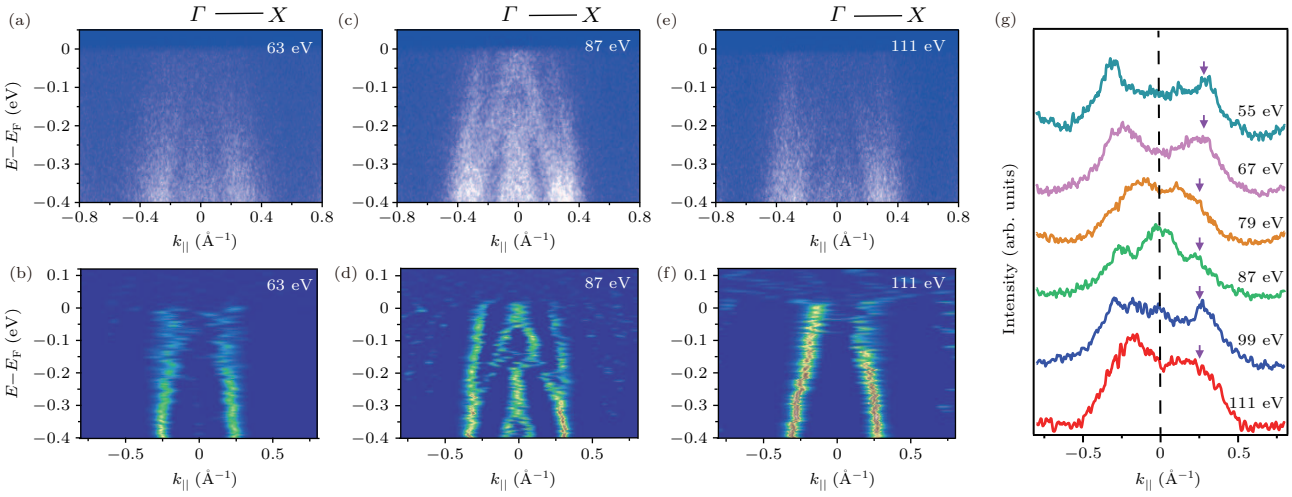


Fig. 3. (a), (c), and (e) Photoemission intensity distributions measured along Γ–X at photon energies of 63 eV, 87 eV, and 111 eV, respectively. (b), (d), and (f) Second-derivative images of the corresponding intensity distributions in panels (a), (c), (e). Second-derivative processing is employed to enhance weak or overlapping band dispersion features, facilitating the identification of subtle electronic structure details (e.g., faint band edges or low-intensity states). (g) Momentum distribution curves (MDCs) extracted from photoemission intensity data across the photon energies studied. Each MDC is obtained by integrating spectral intensity over an energy window of [0,−0.15 eV]. Peaks in the MDCs correspond to the Fermi momentum (k_F) of distinct bands, with arrow markers highlighting the β band's persistent k_F across energies.

A broader survey of Fermi surfaces and band structures across high-symmetry planes of the 115 system ($LaRhIn_5$, $CeRhIn_5$, $SmCoIn_5$) reveals shared features: all exhibit 3D Fermi surfaces comprising both electron-type and hole-type pockets, centered at the high-symmetry points.[46,48,49] Notably, the Fermi surface shape evolves from the square-like to circular-like around the M and A points across these compounds. Despite these commonalities, the contribution of rare-earth 4f electrons to the electronic structure varies markedly among 115 compounds: $LaRhIn_5$ lacks La 4f electrons and features 3D Dirac points in its band structure, though with trivial topology.[46] In $CeRhIn_5$, Ce 4f electrons are partially localized, forming Kondo resonances. Band-dependent hybridization is observed along Γ–M, where the quasi-2D α band shows negligible hybridization, while the 3D γ band exhibits the strongest hybridization.[48] $SmCoIn_5$ has predominantly localized Sm 4f electrons, with hybridization limited to Co 3d/In 5p states at the Z and R points. A global flat band composed of Co 3d states emerges near the Fermi level, potentially arising from geometric frustration.[49] In our measured $GdRhIn_5$, Gd 4f electrons are highly localized: no Dirac points are detected, nor are flat bands from hybridization observed near the Fermi level. These observations suggest that the shared electronic structure features of the 115 systems arise from their layered crystal structure, while differences are governed by the degree of rare-earth 4f localization, crystal field splitting, and hybridization strength. Our interpretation of $GdRhIn_5$'s 3D electronic configuration benefits from comparative electronic structure studies of isostructural $CeRhIn_5$ and first-principles calculations on the parent compound $GdIn_3$, which provide critical contextual insights.[46,48–53]

To investigate the detailed f-band structure, we performed resonant ARPES measurements on $GdRhIn_5$ at the Gd 4f–4d transition edge. On-resonance conditions (tuned to the Gd 4f absorption edge) enhance the spectral weight of states with Gd 4f character, enabling selective probing of f-electron contributions to the band structure.[39] Figures 4(a) and 4(c) present a comparative analysis of ARPES data collected along the Γ–X direction, using LH-polarized light at resonant (150 eV) and off-resonant (110 eV) photon energies, respectively. For reference, the resonance photoemission intensity map acquired along the same Γ–X direction with LV-polarized light (at 150 eV, the resonant energy) is shown in Fig. 4(b). Under resonant conditions, the spectral weight of Gd 4f states is remarkably enhanced. Two key observations confirm this. In the photoemission intensity maps [Figs. 4(a) and 4(b)], a prominent f-derived feature is clearly visible immediately below the Fermi level; this feature is substantially attenuated or absent in the off-resonant LH-polarized data [Fig. 4(c)], where conduction bands (Gd 5d, Rh 5d, In 5p) dominate. The angle-integrated EDCs in Fig. 4(d) exhibit a distinct, sharp peak corresponding to the Gd 4f states — this peak is only pronounced under resonant conditions, further validating the selective enhancement of f-electron spectral weight at 150 eV.

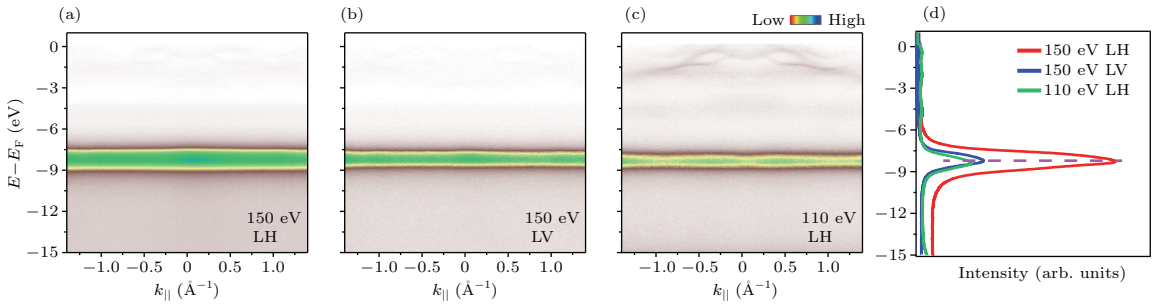


Fig. 4. (a) Photoemission intensity distribution along the Γ–X high-symmetry direction, acquired using on-resonance (150 eV) LH-polarized light. On-resonance conditions (tuned to the Gd 4f absorption edge) enhance the spectral weight of states with Gd 4f character, enabling selective probing of f-electron contributions to the band structure. (b) Photoemission intensity distribution along Γ–X, collected with on-resonance LV-polarized light. (c) Photoemission intensity distribution along Γ–X, measured under off-resonance (110 eV) LH-polarized light. (d) Angle-integrated EDCs extracted from the photoemission intensity data in panels (a)–(c).

Notably, the degree of Gd 4f state enhancement depends strongly on light polarization: LH polarization [Fig. 4(a)] produces a significantly stronger signal for the f-band compared to LV polarization [Fig. 4(b)]. This polarization sensitivity directly reflects the orbital symmetry of Gd 4f states in $GdRhIn_5$ — LH polarization preferentially couples to 4f orbitals with symmetry aligned along the vertical axis of the sample, while LV polarization interacts more weakly with these states. Such polarization-dependent behavior is consistent with the localized nature of the Gd 4f orbitals, whose spatial symmetry is not averaged out by the itinerant hybridization (a key contrast to partially itinerant Ce 4f states in $CeRhIn_5$).

In contrast, resonant ARPES measurements of $CeRhIn_5$ (conducted at the Ce 4f resonance photon energy of 122 eV) reveal three distinct flat bands near the Fermi level, each exhibiting clear spectral dispersion. Among these, the band located 2.32 eV below E_F is assigned to Ce $4f^0$ (empty f-orbital) states, while the bands at 0.27 eV below E_F and in the vicinity of E_F correspond to Ce $4f^1_{7/2}$ and $4f^1_{5/2}$ (singly occupied f-orbital) states, respectively.[48] These features are hallmarks

of partial Ce 4f itinerancy and Kondo hybridization — key characteristics that distinguish Ce-based 115 compounds from Gd-based analogs. Systematic investigations of the broader $Ce_mM_nIn_{3m+2n}$ family (where M = Co, Rh, Ir, Pt; m = 1, 2; n = 0, 1, 2) further demonstrate that $4f^0$ state features are universal across all Ce-containing specimens, manifesting as high-intensity flat bands.[54–62] Notably, both the energy position and spectral intensity of these $4f^0$ bands exhibit substantial material dependence, reflecting variations in Ce 4f-conduction band hybridization strength driven by differences in crystal structure and transition-metal (M) identity. Additionally, weakly dispersive heavy quasiparticle bands near E_F — attributed to hybridized $4f^1_{7/2}$ and $4f^1_{5/2}$ states — show significant intensity variations across this compound family, further underscoring the tunability of Ce 4f itinerancy. Similar weakly dispersive flat bands associated with f-electron hybridization have also been observed in uranium-based heavy fermion compounds such as USb_2, highlighting a common feature of partially itinerant f-electron systems.[63] In stark contrast, Gd-based intermetallic compounds universally exhibit Gd 4f states that are localized at deep binding energies, with minimal hybridization to conduction bands.[64] This fundamental difference arises from the electronic configuration of Gd^{3+} ions: the $4f^7$ shell is half-filled, yielding a total orbital angular momentum $L = 0$ and total spin angular momentum $J = S = 7/2$. The absence of orbital angular momentum ($L = 0$) suppresses crystal electric field effects, as these effects arise from the interaction between the orbital magnetic moment and the lattice's electrostatic potential. With no crystal electric field splitting to destabilize the half-filled shell, Gd 4f orbitals remain tightly localized around the Gd nucleus. Consequently, in our ARPES measurements of $GdRhIn_5$, we observe no evidence of the f-state hybridization features (e.g., $4f^0$ flat bands, heavy quasiparticle bands) that are prominent near E_F in $CeRhIn_5$. This absence directly confirms the strong localization of Gd 4f electrons and their minimal contribution to the low-energy electronic structure — consistent with the broader trend of Gd 4f behavior in gadolinium-based compounds.

In the study of the influence of antiferromagnetic order on the electronic structure of $GdRhIn_5$, variable-temperature ARPES experiments were carried out, with the temperature gradually increased from 7 K to 100 K. At 7 K, significant spectral weights from Gd 5d and In 5p states were observed near the Fermi level, and the γ, β, and σ bands were still present at 100 K. The EDCs data near Γ [Fig. 5(b)] showed that the spectral weights of Gd 5d and In 5p decreased with increasing temperature, although the spectral-weight peaks remained identifiable at 100 K. This phenomenon of decreasing spectral weight with increasing temperature — more intuitively illustrated by the blue line in Fig. 5(d) — is also found in $UFeGa_5$ and $CeCoIn_5$, but the underlying mechanisms differ. In $UFeGa_5$, U 5f electrons become more itinerant as the temperature decreases, and there are no heavy quasiparticle bands due to f–c hybridization near E_F, indicating weak electron correlation.[39] In $CeCoIn_5$, there is obvious f–c hybridization, and Ce 4f electrons transform from localized to partially itinerant states as the temperature decreases, forming a heavy quasiparticle band near E_F. This results in an increased electron density of states, Fermi-surface expansion, and a significant enhancement of the effective mass, showing typical heavy-fermion behavior.[61] In $GdRhIn_5$, the 4f electrons are highly localized, and the energy bands near E_F receive minimal contribution from 4f states. The decrease in spectral weight with increasing temperature may be due to the modulation of Gd 5d/In 5p states by magnetic fluctuations, rather than heavy-fermion behavior, and the inflection point of the change rate [Fig. 5(d)] near T_N supports this hypothesis. When the system approaches the antiferromagnetic ordering temperature T_N, the exchange interaction between local magnetic moments causes the amplitude of spin fluctuations to increase rapidly with rising temperature. These fluctuations introduce additional scattering channels for the 5d/5p conduction electrons via s–d or p–d exchange coupling, directly shortening their quasiparticle lifetime.[65] The integrated ARPES spectral weight is proportional to the quasiparticle peak intensity, so it decreases monotonically as temperature rises and fluctuations intensify. Once the temperature exceeds T_N and the system enters the paramagnetic phase, the antiferromagnetic correlation length decreases,[66] and the modulatory effect of fluctuations on the 5d/5p states tends to saturate, leading to a reduced rate of spectral weight reduction. This behavior originates from the modulation of conduction electron scattering strength in the magnetic order-disorder crossover region and does not involve the formation of heavy quasiparticles due to hybridization between 4f and conduction bands.

In Fig. 5(c), within the energy window of −0.1 eV to −0.2 eV, the peak position of the MDCs near the β band exhibits a general shrink trend as the temperature decreases. This phenomenon, as shown by the red line in Fig. 5(d), can be attributed to the fluctuation-driven redistribution of coherent and incoherent spectral weights. At low temperatures, long-range antiferromagnetic order provides additional coherent scattering channels for Gd 5d/In 5p electrons, allowing ARPES to predominantly detect sharp coherent peaks resulting from exchange splitting. As the temperature increases, the antiferromagnetic correlation length shortens, and the frequency of spin fluctuations exceeds the coherent bandwidth, triggering a redistribution of coherent and incoherent weights: electrons at the same k-point experience rapid spin flips, the weight of the coherent peak decreases, while the weight of the incoherent spectral hump increases accordingly. This enlarges the separa-

tion between the centers of gravity of the two spectral weights, manifesting as peak position shift in the MDC spectrum. The phenomenon of electronic structure changes caused by electronic correlations and the evolution of order parameters has been observed in ARPES studies of various quantum materials, such as CrSBr, CeSb, Fe_3GeTe_2.[67–69]

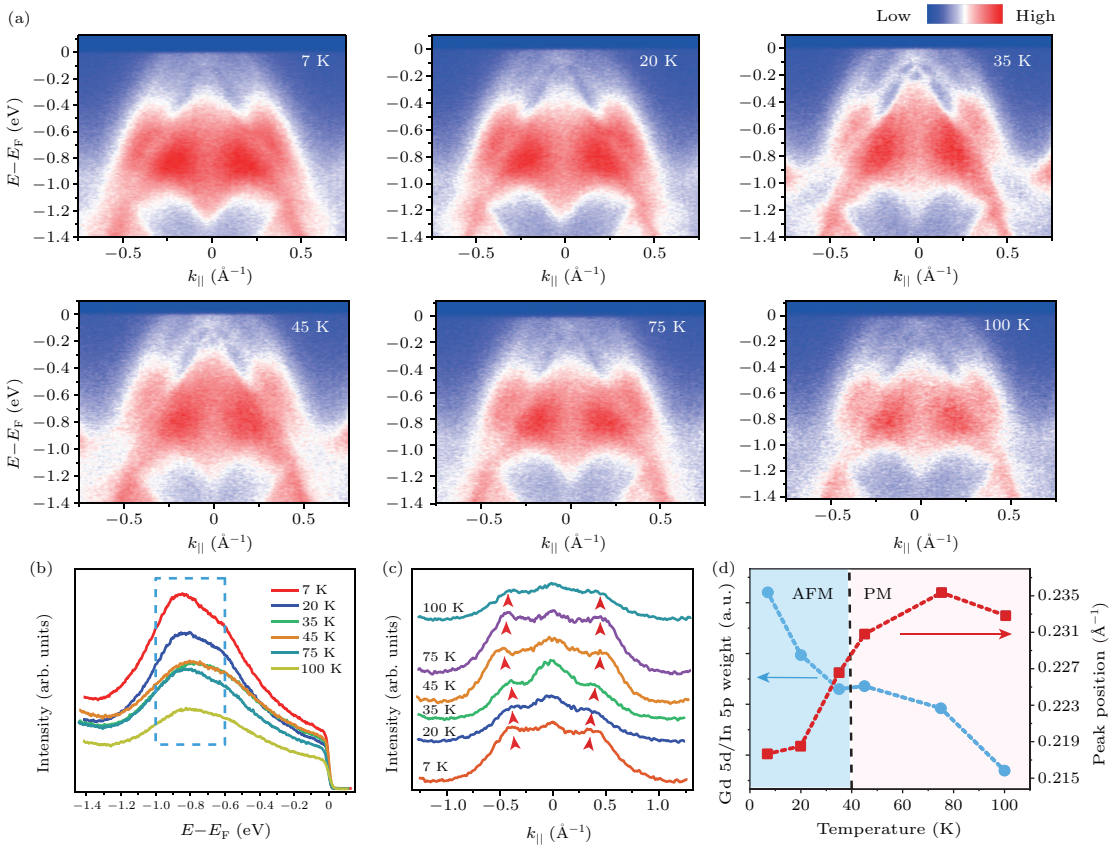


Fig. 5. (a) The temperature dependence of the photoemission intensity distributions of $GdRhIn_5$ along the Γ–X direction at a photon energy of 84 eV, where the temperature gradually increases from 7 K to 100 K. (b) The temperature dependent EDCs obtained by integrating the window of [−0.40 Å, 0.40 Å]. (c) The temperature dependent MDCs obtained by integrating the window of [−0.20 eV, 0.02 eV]. (d) The blue line represents the temperature dependence of the Gd 5d/In 5p spectral weight near E_F, derived by integrating the main peak identified in panel (b) over [−1.00 eV, −0.60 eV]. And the red line represents the temperature dependence of the spectral peak position near the β band, obtained by extracting and fitting the right-side peak positions in panel (c).

4. Conclusion

To summarize, we conducted a systematic investigation into the electronic structure of $GdRhIn_5$ utilizing high-resolution ARPES. We observed dispersive energy bands that incorporate Gd 4f electronic states and collectively form the material's Fermi surface. Energy-dependent measurements further revealed the coexistence of both quasi-two-dimensional and three-dimensional Fermi surface topologies. Notably, the experimentally observed electronic structure exhibits excellent agreement with DFT calculations in which Gd 4f electrons are treated as localized. This consistency indicates that Gd 4f states contribute minimally to the electronic structure near the Fermi level. Resonant ARPES measurements confirmed that Gd 4f states are located deep in the valence band, and do not form heavy quasiparticle bands near the Fermi level — unlike the heavy fermion behavior observed in cerium-based 115-series compounds. Temperature-dependent ARPES measurements reveal that raising the temperature reduces the spectral weight of the Gd 5d/In 5p states and shifts the MDC peak near the β band to higher binding energy. This phenomenon arises from enhanced scattering and coherent-incoherent spectral weight redistribution induced by spin fluctuations near T_N, indicating magnetic fluctuation modulation rather than heavy-fermion behavior. A comparative analysis was conducted between $GdRhIn_5$ and other compounds in the "115" series, revealing that while the layered crystal structure of RE-115 compounds provides a universal structural framework, the degree of localization of rare-earth 4f electrons acts as the critical determinant of the divergent electronic structures observed across the series. Overall, our experimental findings advance the microscopic understanding of $GdRhIn_5$'s physical properties and shed light on the broader family of rare-earth 115 systems, clarifying how rare-earth 4f electron localization modulates electronic behavior in these strongly correlated materials.

Acknowledgments

Project supported by the National Key Research and Development Program of China (Grant No. 2022YFA1402201), the National Natural Science Foundation of China (Grant Nos. U2430209, 12122409, and 52394164), the Institute of Materials, China Academy of Engineering Physics (Grant No. TP02202408), and the Fund of Science and Technology on Surface Physics and Chemistry Laboratory (Grant No. XKFZ202304). We thank the Shanghai Synchrotron Radiation Facility (SSRF) of BL09U (https://cstr.cn/31124.02.SSRF.BL09U) for the assistance on ARPES measurements.

References

[1] Stewart G R 1984 *Rev. Mod. Phys.* **56** 755
[2] Pfleiderer C 2009 *Rev. Mod. Phys.* **81** 1551
[3] Si Q, Rabello S, Ingersent K and Smith J L 2001 *Nature* **413** 804
[4] Sarrao J L, Morales L A, Thompson J D, Scott B L, Stewart G R, Wastin F, Rebizant J, Boulet P, Colineau E and Lander G H 2002 *Nature* **420** 297
[5] Liu Q, Shen B, Smidman M, Li R, Nie Z Y, Xiao X Y, Chen Y, Lee H and Yuan H Q 2018 *Sci. China-Phys. Mech. Astron.* **61** 077411
[6] Wu W and Luo J 2018 *Sci. China-Phys. Mech. Astron.* **61** 127407
[7] Shim J H, Haule K and Kotliar G 2007 *Science* **318** 1615
[8] Paschen S, Luhmann T, Wirth S, Gegenwart P, Trovarelli O, Geibel C, Steglich F, Coleman P and Si Q 2004 *Nature* **432** 881
[9] Gegenwart P, Si Q and Steglich F 2008 *Nat. Phys.* **4** 186
[10] Si Q and Steglich F 2010 *Science* **329** 1161
[11] Yang Y F and Li Y 2015 *Acta Phys. Sin.* **64** 217401 (in Chinese)
[12] Hegger H, Petrovic C, Moshopoulou E G, Sarrao J L, Fisk Z and Thompson J D 2000 *Phys. Rev. Lett.* **84** 4986
[13] Petrovic C, Movshovich R, Jaime M, Pagliuso P G, Hundley M F, Sarrao J L, Fisk Z and Thompson J D 2001 *Europhys. Lett.* **53** 354
[14] Bianchi A, Movshovich R, Vekhter I, Pagliuso P G and Sarrao J L 2003 *Phys. Rev. Lett.* **91** 257001
[15] Jiao L, Chen Y, Kohama Y, Graf D, Bauer E D, Singleton J, Zhu J X, Weng Z F, Pang G M, Shang T, Zhang J L, Lee H, Park T, Jaime M, Thompson J D, Steglich F, Si Q M and Yuan H Q 2015 *Proc. Natl. Acad. Sci. USA* **112** 673
[16] Bianchi A, Movshovich R, Jaime M, Thompson J D, Pagliuso P G and Sarrao J L 2001 *Phys. Rev. B* **64** 220504
[17] Kenzelmann M, Strssle T, Niedermayer C, Sigrist M, Padmanabhan B, Zolliker M, Bianchi A D, Movshovich R, Bauer E D, Sarrao J L and Thompson J D 2008 *Science* **321** 1652
[18] Shishido H, Settai R, Harima H and Ōnuki Y 2005 *J. Phys. Soc. Jpn.* **74** 1103
[19] Sarrao J L, Bauer E D, Mitchell J N, Tobash P H and Thompson J D 2015 *Phys. C* **514** 184
[20] Bauer E D, Altarawneh M M, Tobash P H, Gofryk K, Ayala-Valenzuela O E, Mitchell J N, McDonald R D, Mielke C H, Ronning F, Griveau J C, Colineau E, Eloirdi R, Caciuffo R, Scott B L, Janka O, Kauzlarich S M and Thompson J D 2012 *J. Phys.: Condens. Matter* **24** 052206
[21] Petrovic C, Pagliuso P G, Hundley M F, Movshovich R, Sarrao J L, Thompson J D, Fisk Z and Monthoux P 2001 *J. Phys.: Condens. Matter* **13** L337
[22] Movshovich R, Jaime M, Thompson J D, Petrovic C, Fisk Z, Pagliuso P G and Sarrao J L 2001 *Phys. Rev. Lett.* **86** 5152
[23] Park T, Ronning F, Yuan H Q, Salamon M B, Movshovich R, Sarrao J and Thompson J D 2006 *Nature* **440** 65
[24] Helm T, Grockowiak A D, Balakirev F F, Singleton J, Betts J B, Shirer K R, König M, Förster T, Bauer E D, Ronning F, Tozer S W and Moll P J W 2020 *Nat. Commun.* **11** 3482
[25] Pagliuso P G, Thompson J D, Hundley M F, Sarrao J L and Fisk Z 2001 *Phys. Rev. B* **63** 054426
[26] Granado E, Uchoa B, Malachias A, Lora-Serrano R, Pagliuso P G and Westfahl H Jr 2006 *Phys. Rev. B* **74** 214428
[27] Ł ątka K, Kmieć R, Rams M, Pacyna A W, Zaremba V I and Pöttgend R 2004 *Zeitschrift für Naturforschung B* **59** 947
[28] Khalladi R, Mtougui S, Idrissi S, Bahmad L, Ziti S and Labrim H 2018 *Chin. J. Phys.* **56** 2937
[29] Czjzek G, Oestreich V, Schmidt H, Łątka K and Tomala K 1989 *J. Magn. Magn. Mater.* **79** 42
[30] Hoffmann R D, Pöttgen R, Fickenscher Th, Felser C and Łątka K and Kmieć R 2002 *Solid State Sci.* **4** 609
[31] Ł ątka K, Tomkowicz Z, Kmieć R, Pacyna A W, Mishra R, Fickenscher Th, Hoffmann R D and Pöttgen R 2002 *J. Solid State Chem.* **168** 331
[32] Lora S R, Garcia D J, Betancourth D, Amaral R P, Camilo N S, Estévez-Rams E, Ortellado G Z and Pagliuso P G 2016 *J. Magn. Magn. Mater.* **405** 304
[33] Zhang J H, Liu L, Gu F, Yang L J and Liu M 2006 *Acta Phys. Sin.* **55** 2928 (in Chinese)
[34] Kandpal H C, Casper F, Fecher G H, Felser C, Kübler J and Pöttgen R 2007 arXiv:0709.4445 [physics.comp-ph]
[35] Johansson B and Li S 2009 *Philos. Mag.* **89** 1793
[36] Dong X P, Zhao X, Yin L H, Peng S Q, Wang J N and Guo Y Q 2023 *Acta Phys. Sin.* **72** 107501 (in Chinese)
[37] Facio J I, Betancourth D, Pedrazzini P, Correa V F, Vildosola V, García D J and Cornaglia P S 2015 *Phys. Rev. B* **91** 014409
[38] Thompson J D and Fisk Z 2011 *J. Phys. Soc. Jpn.* **81** 011002
[39] He X W, Luo X B, Wang B, Feng W, Yuan D P, Liu Y, He Y L, Liu Z T, Shen D W, Ye M, Liu J S, Liu Q, Huang Y B, Hao Q Q, Yang X F, Zhang Y, Tan S Y, Chen Q Y and Lai X C 2025 *Phys. Rev. B* **112** 205109
[40] Szade J and Neumann M 1999 *J. Phys.: Condens. Matter* **11** 3887
[41] Szade J and Neumann M 2001 *J. Phys.: Condens. Matter* **13** 2717
[42] Moreno N O, Bauer E D, Sarrao J L, Hundley M F, Thompson J D and Fisk Z 2005 *Phys. Rev. B* **72** 035119
[43] Chen Y L 2012 *Front. Phys.* **7** 175
[44] Damascelli A 2004 *Phys. Scr.* **T109** 61
[45] Damascelli A, Hussain Z and Shen Z X 2003 *Rev. Mod. Phys.* **75** 473
[46] Wang Y Z, Li T R, Xu R, Yao J H, Liao S, Liu Z T, Shen D W, Zhang Y J, Chen Q Y, Wang Y L, Jiang J and Feng D L 2025 *Phys. Rev. B* **112** 035122
[47] Berbil-Bautista L, Hänke T, Getzlaff M, Wiesendanger R, Opahle I, Koepernik K and Richter M 2004 *Phys. Rev. B* **70** 113401
[48] Chen Q Y, Xu D F, Niu X H, Peng R, Xu H C, Wen C H P, Liu X, Shu L, Tan S Y, Lai X C, Zhang Y J, Lee H, Strocov V N, Bisti F, Dudin P, Zhu J X, Yuan H Q, Kirchner S and Feng D L 2018 *Phys. Rev. Lett.* **120** 066403
[49] Tam D W, Colonna N, Strocov V N, Gawryluk D J, Pomjakushina E and Kenzelmann M 2024 *npj Quantum Mater.* **9** 26
[50] Moore D P, Durakiewicz T, Joyce J J, Arko A J, Morales L A, Sarrao J L, Pagliuso P G and Wills J M 2002 *Phys. B* **312** 134
[51] Fujimori S 2016 *J. Phys.: Condens. Matter* **28** 153002
[52] Yin Z X, Du X, Zhang S, Chen C, Pei D, Zhou J S, Gu X, Xu R Z, Zhang Q Q, Zhao W X, Li Y D, Xu Y F, Bernevig A, Liu Z K, Liu E K, Chen Y L and Yang L X 2022 *Phys. Rev. Mater.* **6** 084203
[53] Shafiq M, Ahmad I and Asadabadi S J 2014 *J. Appl. Phys.* **116** 103905
[54] Fujimori S, Okane T, Okamoto J, Marniya K, Muramatsu Y, Fujimori A, Harima H, Aoki D, Ikeda S, Shishido H. Tokiwa Y, Haga Y and Onuki Y 2003 *Phys. Rev. B* **67** 144507
[55] Duan Y X, Zhang C, Rusz J, Oppeneer P M, Durakiewicz T, Sassa Y, Tjernberg O, Mansson M, Berntsen M H, Wu F Y, Zhao Y, Song J J, Wu Q Y, Luo Y, Bauer E D, Thompson J D and Meng J Q 2019 *Phys. Rev. B* **100** 085141
[56] Patil S, Generalov A, Guttler M, Kushwaha P, Chikina A, Kummer K, Rodel T C, Santander-Syro A F, CarocaCanales N, Geibel C, Danzenbacher S, Kucherenko Y, Laubschat C, Allen J W and Vyalikh D V 2016 *Nat. Commun.* **7** 11029
[57] Yao Q, Kaczorowski D, Swatek P, Gnida D, Wen C H P, Niu X H, Peng R, Xu H C, Dudin P, Kirchner S, Chen Q Y, Shen D W and Feng D L 2019 *Phys. Rev. B* **99** 081107
[58] Yuan Y H, Duan Y X, Rusz J, Zhang C, Song J J, Wu Q Y, Sassa Y, Tjernberg O, Mansson M, Berntsen M H, Wu F Y, Liu S Y, Liu H, Zhu S X, Liu Z T, Zhao Y Z, Tobash P H, Bauer E D, Thompson J D, Oppeneer P M, Durakiewicz T and Meng J Q 2021 *Phys. Rev. B* **103** 125122
[59] Zhang Y, Feng W, Lou X, Yu T L, Zhu X G, Tan S Y, Yuan B K, Liu Y, Lu H Y, Xie D H, Liu Q, Zhang W, Luo X B, Huang Y B, Luo L Z, Zhang Z J, Lai X C and Chen Q Y 2018 *Phys. Rev. B* **97** 045128
[60] Liu H J, Xu Y J, Zhong Y G, Guan J Y, Kong L Y, Ma J Z, Huang Y B, Chen Q Y, Chen G F, Shi M, Yang Y F and Ding H 2019 *Chin. Phys. Lett.* **36** 097101

[61] Chen Q Y, Xu D F, Niu X H, Jiang J, Peng R, Xu H C, Wen C H P, Ding Z F, Huang K, Shu L, Zhang Y J, Lee H, Strocov V N, Shi M, Bisti F, Schmitt T, Huang Y B, Dudin P, Lai X C, Kirchner S, Yuan H Q and Feng D L 2017 *Phys. Rev. B* **96** 045107
[62] Chen Q Y, Wen C H P, Yao Q, Huang K, Ding Z F, Shu L, Niu X H, Zhang Y, Lai X C, Huang Y B, Zhang G B, Kirchner S and Feng D L 2018 *Phys. Rev. B* **97** 075149
[63] Chen Q Y, Luo X B, Xie D W, Ji X Y, Zhou R, Huang Y, Zhang W, Feng W, Zhang Y, Huang L, Hao Q Q, Liu Q, Zhu X, Liu Y, Zhang P, Lai X, Si Q and Tan S Y 2019 *Phys. Rev. Lett.* **123** 106402
[64] Shikin A M, Estyunin D A, Surnin Yu I, Koroleva A V, Shevchenko E V, Kokh K A, Tereshchenko O E, Kumar S, Schwier E F, Shimada K, Yoshikawa T, Saitoh Y, Takeda Y and Kimura A 2019 *Sci. Rep.* **9** 4813
[65] Watson M D, Markovic I, Mazzola F, Rajan A, Morales E A, Burn D M, Hesjedal T, van der Laan G, Mukherjee S, Kim T K, Bigi C, Vobornik I, Hatnean M C, Balakrishnan G and King P D C 2020 *Phys. Rev. B* **101** 205125
[66] Luo H Q, Zhang R, Laver M, Yamani Z, Wang M, Lu X Y, Wang M Y, Chen Y C, Li S L, Chang S, Lynn J W and Dai P C 2012 *Phys. Rev. Lett.* **108** 247002
[67] Wu F, Zhang X F, Chen Y, Pei D, Zhan M W, Tao Z C, Chen C, Lu S P, Chen J Z, Tang S J, Wang X, Guo Y F, Yang L X, Zhang Y, Chen Y L, Mi Q X, Li G and Liu Z K 2025 *Sci. China Phys. Mech. Astron.* **68** 267411
[68] Li T R, Liu Z F, Li P, Wang Y Z, Zhao Z S, Su S W, Jiang Z C, Hong Y H, Tian H, Zheng X, Liu Y, Wang Y L, Liu Z T, Shen D W, Sun Z, Liu Y, Jiang J and Feng D L 2025 *Commun. Mater.* **6** 97
[69] Sharma D, Ali A, Bhatt N, Chowdhury R R, Patra C, Singh R P and Singh R S 2024 *Phys. Rev. B* **110** 125119